Moiré pattern in scanning tunneling microscopy: Mechanism in observation of subsurface nanostructures

Katsuyoshi Kobayashi
Department of Physics, Graduate School of Science, University of Tokyo, 7-3-1 Hongo, Bunkyo-ku, Tokyo 113, Japan
(Received 8 December 1995)

The origin of moiré patterns in scanning tunneling microscopy (STM) is clarified. It is found that two factors are important in observing the moiré patterns in STM. One is interface scattering in lattice-mismatched systems, which produces nanoscale lateral waves. The other is a qualitative difference of decay behavior in the vacuum region between the nanoscale and atomic-scale lateral waves, because of the typical value of work functions. Different from those in transmission electron microscopy (TEM), the moiré patterns in STM are not the beat of waves but are essentially due to three-dimensional tunneling. Furthermore, it is found that the nanoscale waves propagate through many layers without decay due to the typical value of Fermi energies. This means that nanoscale structures can be observed in STM even if they are buried deep in surfaces. These findings are evidently demonstrated by numerical calculations. The mechanism of this paper clarifies conditions for obtaining subsurface information by STM.

I. INTRODUCTION

Since its invention, scanning tunneling microscopy (STM) has been used extensively for studying topography and electronic states of surfaces. Interest in most of the studies has been concentrated on outermost layers of surfaces, because inner layers are usually not observed in STM. However, several STM experiments showing information of the inner layers have been reported recently. For example, moiré patterns have been observed in STM of lattice-mismatched systems.[1–15] Images of bulk defects buried in semiconductor surfaces have been observed clearly in STM.[16–18]

These observations of the subsurface structures in STM are quite curious from a theoretical point of view. According to the Tersoff and Hamann theory,[19] STM images reflect local density of states (LDOS) of surfaces in the vacuum region. This means that STM images are very sensitive to electronic states of only outermost layers of surfaces. As Tersoff and Hamann showed for the Au(110) surface,[19] STM images are usually quite insensitive to atomic structures of inner layers. However, subsurface structures such as the moiré patterns and bulk defects are observed in STM. Moreover, corrugation amplitudes of the subsurface structures are often larger than those of atomic structures.[2,3,18]

In this paper, we discuss and clarify the origin of the observation of subsurface structures in STM, mainly focusing on the moiré patterns. The most important conclusion of this paper is that subsurface structures are generally visible in STM if they have nanoscale dimensions. Furthermore, STM can observe nanoscale structures even if they are buried deep in subsurfaces. These results are due to two facts. One is that STM makes use of the three-dimensional tunneling phenomenon. The other is that characteristic lengths of work functions and Fermi energies of most materials lie between the atomic scale and the nanoscale.

Moiré patterns are often observed in STM when lattice constants of overlayers and substrates are slightly different. Usually, the moiré patterns have been explained by simple superposition of atomic structures of the overlayers and substrates. This interpretation would be the analogy of transmission electron microscopy (TEM). In TEM images, moiré patterns are often observed, when electrons are transmitted through two layers with slightly different lattice constants. The moiré patterns in TEM are explained in terms of the beat of two waves with slightly different frequencies. However, it is questionable that this picture is also applicable to the moiré patterns in STM, because STM makes use of tunneling phenomenon. In this picture, electrons tunnel directly from inner layers of surfaces as well as from outermost layers, but the meaning of the direct tunneling from inner layers is not clear.

Another picture for the moiré patterns in STM is that electronic structures of overlayers are modulated by influence of lattice-mismatched substrates. However, this picture is not sufficient, because moiré patterns are observed in layered materials such as graphite[1–5] and transition-metal dichalcogenides.[9,10] In these materials, interlayer interaction is very weak and, therefore, the influence of substrates on overlayers would be small. Moreover, moiré patterns are clearly observed even when four monolayers of $MoSe_2$ are grown on a MoS_2 substrate.[10] To explain these facts, the modulation of electronic structures in overlayers alone would not be sufficient.

In lattice-mismatched systems, atomic positions of overlayers are modulated by the influence of substrates. There is a standpoint that moiré patterns in STM are explained by the modulation of the atomic structures of overlayers. However, moiré patterns have not been observed by atomic force microscopy (AFM) as far as the present author knows. Moreover, corrugation amplitudes of moiré patterns are usually much larger than those expected from small atomic displacements. These facts imply the importance of electronic effects in moiré patterns in STM.

In this paper, we present a picture for the observation of the moiré patterns in STM. In the next section, we discuss the origin of the moiré patterns qualitatively, where it is clarified that moiré patterns in STM are essentially due to

three-dimensional tunneling and are quite different from those in TEM. This mechanism is verified by numerical calculations in Sec. III, where it is shown that the moiré patterns are obtained even if interfaces of the overlayers and substrates are buried deep in subsurface. In Sec. IV, discussion and conclusion are presented. In this paper, we use atomic units ($\hbar=m=e=1$) if units are not shown explicitly.

II. ORIGIN OF MOIRÉ PATTERNS IN SCANNING TUNNELING MICROSCOPY

In this section, we present a qualitative picture for the moiré patterns in STM. For this purpose, we discuss scattering behavior of electrons in detail.

Behavior of electrons transmitted through matter depends on the kinetic energy of incident electrons. When the kinetic energy is much larger than strength of the scattering potential in the matter, the perturbative treatment is valid. In this case, the Born approximation is good, and wave functions of the transmitted electrons are expressed in terms of superposition of waves singly scattered by each atomic potential. Therefore, high-energy electrons transmitted through two layers with slightly different lattice constants show moiré patterns, as seen in TEM images. The typical kinetic energy of the electrons is 100 keV.

When the kinetic energy of electrons is lowered to the same order with the potential strength, the effect of multiple scattering manifests itself. In this case, wave functions of the scattered electrons cannot be expressed by the simple superposition of singly scattered waves. Interpretation of images is complicated.

Another factor determining the scattering behavior of low-energy electrons is the channeling. Because of the conservation of the kinetic energy, propagating channels of the scattered electrons are restricted. For example, when the kinetic energy is E, channels with lateral momenta larger than $\sqrt{2E}$ do not propagate in the direction normal to the surface. Therefore, no atomic image is observed on a screen far from a sample surface when $E<(2\pi/a)^2/2$, where a is a lattice constant of the sample. However, when the electrons transmit through two layers with slightly different lattice constants a and b, they can gain a small lateral momentum of $2\pi/l=|2\pi/a-2\pi/b|$ by the multiple scattering. Therefore, a structure with the period of l is observed if $E>(2\pi/l)^2/2$. In this case, different from the high-energy electrons, the image shows not a moiré pattern but only a superstructure with the period of l.

In the case of tunneling, there is no propagating channel and all waves decay in the vacuum region. Therefore, the probe in STM must be situated near sample surfaces. The typical tip-sample distance is 10 Å. Since the kinetic energy of electrons at the Fermi level is the same order as the potential strength, the multiple scattering is also important in this case. A simple and useful interpretation of STM images has been given by Tersoff and Hamann.[19] In their theory, the tunneling current is proportional to the Fermi-level LDOS of a sample surface at the position of the tip. Since electronic states in the vacuum region are very sensitive to only outermost layers, STM images reflect usually atomic structures of the outermost layers. Therefore, it seems that even when the lattice constants of the outermost and second layers are slightly different, moiré patterns such as those in high-energy TEM cannot be observed in STM. However, moiré patterns are observed in STM on account of another kind of mechanism, explained as follows.

The main component of wave functions in the vacuum region near the outermost layer is the wave with the lateral momentum of $2\pi/a$. The component with the lateral momentum of $2\pi/l$ produced by the multiple scattering is a higher-order term and its amplitude is generally very small. However, waves with larger lateral momenta decay faster, because a wave with a lateral momentum q decays in the vacuum region as

$$\exp(-\lambda z), \quad \lambda\equiv\sqrt{2|E|+q^2}, \tag{2.1}$$

where E is the energy of the wave function measured from the vacuum level, and z axis is perpendicular to the surface. Therefore, even if the amplitude is small in the region of the outermost layer, the large lateral structure of l is observed in STM when the tip is scanned far from the sample surface. If the tip-sample distance is properly chosen, the large lateral structure and the atomic structure are observed simultaneously. This is the moiré pattern observed in STM.

If we use 5 a.u., 20 a.u., and 5 eV as typical values of the atomic lattice spacing a, nanoscale structure l, and work function $|E|$, the energies of $(2\pi/a)^2/2$, $(2\pi/l)^2/2$, and $|E|$ are calculated as 0.8, 0.05, and 0.2, respectively. Therefore, the decay behavior in the vacuum region is different between the atomic-scale and nanoscale waves. As seen from Eq. (2.1), the decay constant of the former is governed by the lattice spacing and the latter is by the work function. The border of these scales is about 5 Å for the typical work function of 5 eV.

According to the Tersoff and Hamann theory,[19] the corrugation amplitude Δz decays exponentially with increase of the tip-sample distance as

$$\Delta z\sim\frac{1}{\lambda_0'}\exp[-2(\lambda'-\lambda_0')z], \quad \lambda'\equiv\sqrt{2|E|+\frac{q^2}{4}}, \tag{2.2}$$

where λ_0' is the value of λ' for $q=0$. However, the corrugation amplitude of nanoscale structures does not decay within the ordinary tip-sample distance observing STM images, because the decay constant of nanoscale structures is almost the same as that of the component with $q=0$. The constant corrugation amplitude of nanoscale structures is observed in an STM experiment of an Al(111)-S surface,[15] where the decay of the atomic corrugation with the tip-sample distance is also observed.

If we use Eq. (2.2) and the above typical values for calculating the corrugation amplitudes of the nanoscale structure Δz_l and the atomic-scale structure Δz_a, we find that the ratio $\Delta z_l/\Delta z_a$ is enhanced by a factor of 12 with increase of the tip-sample distance by 5 a.u. This means that nanoscale structures are generally visible in STM even when the amplitude of the nanoscale structures is negligibly small at the region of the outermost layers.

The fact that smaller structures decay faster than larger structures has already been pointed out in the early work by Tersoff and Hamann,[19] but it has been used for discussing only atomic-scale structures of outermost layers. In this paper, it is used from a different point of view for explaining

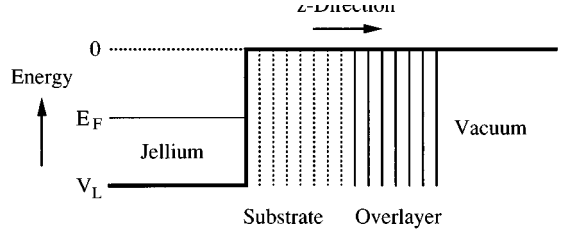

FIG. 1. Schematic of the model system used in the numerical calculations.

the observation of subsurface structures in STM, where the typical value of work functions is important to discriminate qualitatively the decay behavior of nanoscale and atomic-scale structures.

The qualitative difference between nanoscale and atomic-scale structures is also remarkable in the case of electrons propagating through inner layers of surfaces. Since the typical Wigner-Seitz radius r_s is 3.0 a.u., the Fermi energy $k_F^2/2=(9\pi/4)^{2/3}/(2r_s^2)$ is 0.2. This value is the same order as that of the typical work function and smaller than the lateral kinetic energy $(2\pi/a)^2/2(=0.8)$ of atomic-scale structures. Therefore, atomic-scale waves cannot propagate in a structureless jellium which is a spatial average of atomic potentials. In a real crystal, the atomic-scale waves have a finite amplitude only around the region of atoms by the scattering of the atomic potentials from the $q=0$ component. Therefore, these waves decay rapidly on an atomic scale in the regions of the vacuum and lattice-mismatched interfaces. This is the reason why subsurface atomic-scale structures are generally not observed in STM.

In contrast, the lateral kinetic energy of nanoscale structures is smaller than the Fermi energy. Therefore, nanoscale waves can propagate through many layers without decay. In other words, nanoscale waves behave like the $q=0$ component. This means that information of interfaces buried deep in subsurfaces can be obtained in STM mediated by nanoscale waves.

III. NUMERICAL CALCULATIONS

A. Method of calculation

To verify the discussions in the preceding section, we perform numerical calculations for a realistic system. Our aim is not to treat a specific case but to discuss general features semiquantitatively. Figure 1 shows a schematic of the model system used in the present calculations. We use the screened empty-core pseudopotential[20] for the atomic potential given by

$$V(\mathbf{r})=\begin{cases} -\dfrac{e^{-\kappa_s r}}{r} & (r>r_c) \\ 0 & (r<r_c). \end{cases} \tag{3.1}$$

For the overlayer, we choose a Cu(111) surface as a typical example. The lattice constant, r_c, and κ_s are 4.83, 0.81, and 0.9, respectively.[20] We use a 10×10 supercell for calculating moiré patterns. Then, the lattice constant of the supercell is 48.3 a.u. The lattice vectors of the overlayer and substrate are aligned and the lattice constant of the substrate is chosen so that the 9×9 supercell is commensurate with the 10×10 supercell of the overlayer. For r_c and κ_s of the substrate, we use values of 0.9 and 0.81, respectively, because the ratio of the lattice constants of the substrate and overlayer is 10/9.

Transmission images are calculated for a system where both the overlayer and substrate are monolayers. In calculating STM images, the number of layers in the overlayer is varied from 1 to 10 for investigating dependence of moiré patterns on the overlayer thickness. The number of layers in the substrate is fixed as 5. Atoms are arranged in the hcp structure. The structure of the lattice-mismatched interface is chosen so that one of the atoms in the overlayer is put on the top of one of the atoms in the substrate. In these calculations, all the interlayer distances are fixed as 4.0 a.u. and the bottom of the substrate is situated at the position by 1.0 a.u. above the edge of the jellium for reducing the unphysical interface scattering by joining smoothly the substrate and jellium.

Energies are measured from the vacuum level. Since the work function of Cu is about 4.5 eV, the Fermi energy E_F is chosen as -0.15. The bottom energy of the jellium V_L is set at -0.192 which is a spatially averaged value of the substrate atomic potentials. In the calculations of TEM images, we set $V_L=0$. In the present model, the lateral kinetic energies corresponding to the atomic spacings of the overlayer and substrate are $E_1=1.1$ and $E_2=0.9$, respectively.

Wave functions are solved by the recursion-transfer-matrix method,[21] which enables us to obtain an accurate tail part of the wave functions in the vacuum region without the difficulty of divergence. The cutoff energy for the lateral kinetic energy is chosen as 1.5. This is too small to express accurately waves with shorter wavelengths than the atomic spacing, but is sufficient for the present purpose of the comparison between the nanoscale and atomic-scale structures. The intervals of mesh points along the z axis are 0.5 and 0.1 a.u. in the calculations of STM and TEM images, respectively.

TEM images are calculated from only the channel with the direction of incident electrons normal to the surface. Wave functions are calculated at the position by 10.0 a.u. above the outermost layer. Components decaying in the vacuum region are omitted, because TEM images in experiments are observed on a screen far from sample surfaces. STM images are calculated by the Tersoff and Hamann formula using the LDOS $\rho(\mathbf{r},E)$ at the Fermi level.[19] In the case of the large unit-cell system, the two-dimensional integral in the reciprocal space is replaced by a sum of the channels with a weight as

$$\rho(\mathbf{r},E)=\frac{2S}{(2\pi)^3}\sum_{|\mathbf{G}_\parallel|<\sqrt{2(E-V_L)}}\frac{|\psi_{E,\mathbf{G}_\parallel}(\mathbf{r})|^2}{\sqrt{2(E-V_L)-\mathbf{G}_\parallel^2}}, \tag{3.2}$$

where $\psi_{E,\mathbf{G}_\parallel}$ is a wave function with an energy E and a two-dimensional reciprocal lattice vector $\mathbf{G}_\parallel$. S is the area of the first Brillouin zone.

B. TEM image

Figure 2 shows calculated TEM images. The images are displayed in a 2×2 supercell of the present unit cell. Figure 2(a) is an image for $E=100$. In the case of the high-energy

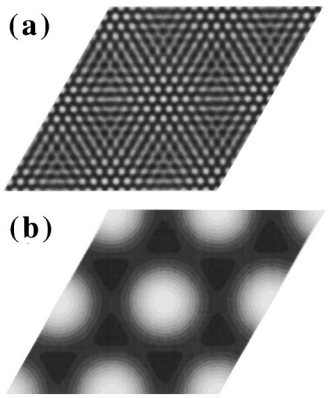

FIG. 2. Calculated TEM images. The energy E of the incident electron is (a) 100 and (b) 0.5. V_L is set to 0.

transmission, the calculated image shows a moiré pattern which can be interpreted as a beat produced by superposing two waves with slightly different periods. The two waves also beat along the z axis because of the conservation of kinetic energies. The period of the beat is about 400 a.u. in the present case, because the difference of the momenta normal to the surface is given by $|E_1-E_2|/\sqrt{2E}$ for the high-energy electron. The moiré pattern is obtained in the energy region of $E>E_1$.

When $E_1>E>E_2$, calculated images show the atomic structure of the substrate. In this case, the overlayer has only the $q=0$ component in the scattering potential and behaves like a structureless sheet. When $E<E_2$, calculated images show no atomic structure but only a superstructure with a long period of the present unit cell. Figure 2(b) shows a calculated image for $E=0.5$. This image is calculated from only the channel with the incident direction normal to the surface. If a summation is taken over all the incident channels, calculated images show atomic structures. Even when $E<E_2$, a wave $\mathbf{q}$ with an atomic period is produced by the interference terms of $\mathbf{q}/2$ and $-\mathbf{q}/2$ components, in calculating the absolute square of a wave function. When $E<E_2/4$, calculated images show no atomic structure for all the channels.

C. STM image

In the energy region of tunneling, STM images show moiré patterns, depending on the tip-sample distance. Figure 3 shows calculated STM images. These images are calculated for the case that the overlayer thickness is one layer and $E=E_F(=-0.15)$. The position of the LDOS is by (a) 1.0, (b) 3.0, and (c) 5.0 a.u. above the outermost layer. When the tip-sample distance is short, only the atomic structure of the outermost layer is seen as Fig. 3(a). As the distance increases, the moiré pattern becomes distinct.

In the present calculations, STM images are evaluated from the LDOS of the surfaces using the Tersoff and Hamann theory.[19] This corresponds to STM images that are observed by an s-wave tip. As has been shown by Chen, the d-wave tip is important for explaining the large atomic corrugation of metal surfaces.[22] In the present calculations, the effect of the d-wave tip can be taken into account easily according to Chen's formula.[22] STM images are calculated

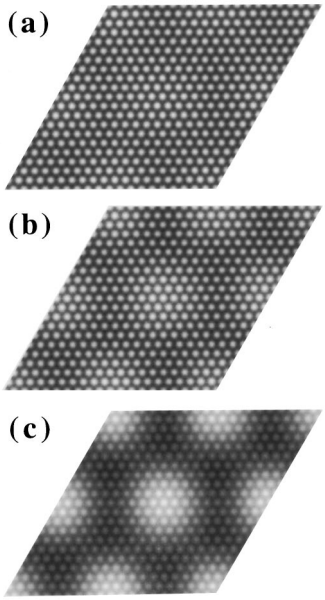

FIG. 3. Calculated STM images. The overlayer thickness is one layer. The energy E of the electron is $-0.15(=E_F)$. V_L is set to -0.192. The position of the tip is by (a) 1.0, (b) 3.0, and (c) 5.0 a.u. above the outermost layer. As the tip-sample distance increases, the moiré pattern becomes distinct.

by multiplying each component of the wave functions in the vacuum region by a factor which is a function of the decay constant. The result is that atomic-scale structures are enhanced by the d-wave tip but nanoscale structures are not enhanced, because the decay constant of nanoscale waves are almost the same as that of the $q=0$ component. This means that the position of the tip observing moiré patterns becomes far from the surface in the case of the d-wave tip.

The moiré pattern is clearly visible even for six layers of the overlayer thickness. Figure 4 shows STM images calculated for the cases that the overlayer thickness is (a) 2 and (b) 6 layers. The tip-sample distance is 5.0 a.u. and $E=E_F$. In the two-layer case shown in Fig. 4(a), the contrast of the superstructure is reversed.

This behavior of the STM images depending on the overlayer thickness is due to the standing wave formed by the

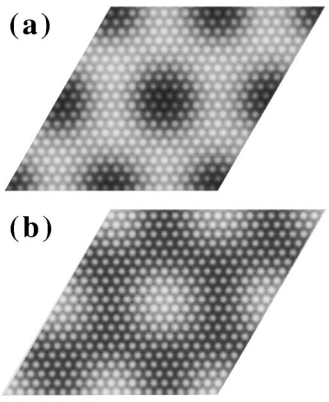

FIG. 4. Calculated STM images. The overlayer thickness is (a) two and (b) six layers. The energy E is E_F. The position of the tip is by 5.0 a.u. above the outermost layer.

total reflection at the surface. Figure 5(a) shows variations of amplitudes of the superstructure, the atomic structures of the overlayer and substrate, and the $q=0$ component along the z axis. Here, the superstructure means the wave with the long wavelength of the present unit cell. The amplitudes are calculated by Fourier transformation from the absolute square of a wave function with a single incident channel normal to the surface. The overlayer thickness is four layers and $E=E_F$. Values are shown in the unit of the incident wave. The unit of the horizontal axis is the interlayer distance $d(=4.0)$ and the position of the outermost layer is zero.

In Fig. 5(a), the $q=0$ component shows oscillating behavior. This is a standing wave with a period of $2k_F$ formed as

$$\left|e^{ik_Fz}-e^{-ik_Fz}\right|^2 \propto 1-\cos(2k_Fz). \tag{3.3}$$

In the present case, the period π/k_F calculated from a spatial average of the scattering potential in the overlayer is 10.8 a.u. (=2.7 layers) which agrees well with the period in Fig. 5(a).

The period of the superstructure is slightly longer than that of the $q=0$ component, because k_z of the superstructure is slightly smaller than k_F due to the lateral kinetic energy. By a simple model using a δ-function potential, it can be shown that spatial variation of the superstructure amplitude along the z axis is given by

$$\sin(k_Fz)\sin(k_F'z)=\frac{\cos[(k_F-k_F')z]-\cos[(k_F+k_F')z]}{2}, \tag{3.4}$$

where $k_F'=\sqrt{k_F^2-q^2}$ and q is the lateral momentum of the superstructure. The derivation is shown in the Appendix. If $k_F'=k_F$, this is the same as Eq. (3.3). By the slight difference between k_F' and k_F, the wave of the superstructure shows the behavior slightly different from the $q=0$ component. For example, the negative amplitude of the superstructure around $z/d=-2$ in Fig. 5(a) is explained by Eq. (3.4).

The components corresponding to the atomic structures of the overlayer and substrate also show the oscillating behavior in Fig. 5(a). In this case, the period of the oscillation is the same as that of the $q=0$ component, because the atomic-scale waves are produced only by the scattering of the atomic potential from the $q=0$ component and decay in the structureless jellium. Their standing-wave behavior is due to that of the $q=0$ component, and their amplitudes are proportional to that of the $q=0$ component. In contrast, the nanoscale wave of the superstructure produced by the interface scattering propagates through the overlayer and is reflected by the surface. Therefore, the standing-wave behavior of the superstructure bears no relation to the $q=0$ component, and the period is slightly different from that of the $q=0$ component.

In calculating the LDOS, all the channels must be taken into account. Figure 5(b) shows amplitudes calculated from the LDOS for the case that the overlayer thickness is four layers and $E=E_F$. The amplitudes displayed are normalized by the $q=0$ component. Therefore, the standing-wave behavior is hidden. The amplitude of the substrate atomic structure decays rapidly on an atomic scale at the interface, and the amplitude of the overlayer grows instead. The amplitude of the superstructure produced at the interface propagates through the overlayer without decay and is detected by STM

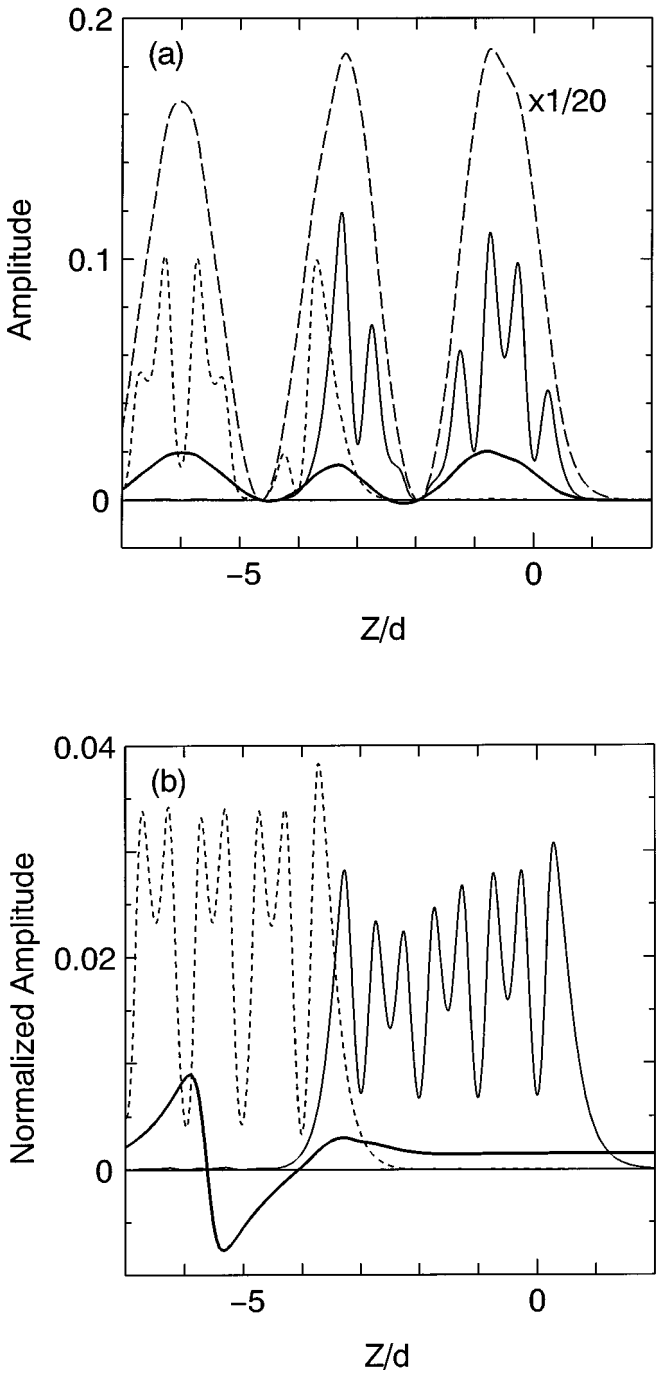

FIG. 5. Variation along the z axis of the amplitudes of waves corresponding to the superstructure (heavy solid line), the atomic structures of the overlayer (solid line) and substrate (dotted line), and the $q=0$ component (broken line). The amplitudes are calculated by Fourier transformation from (a) an absolute square of a wave function with a channel of the incident wave normal to the surface and (b) the LDOS. Values are displayed in the unit of the incident wave in (a) and are normalized by the $q=0$ component in (b). The overlayer thickness is four layers. The unit of the horizontal axis is the interlayer distance $d(=4.0$ a.u.), and the position of the outermost layer of the overlayer is zero. Therefore, -3.0 and -4.0 are the positions of the lowermost layer of the overlayer and the outermost layer of the substrate, respectively. Values of the $q=0$ component in (a) are scaled down by 1/20.

in the vacuum region, due to the rapid decay of the overlayer atomic structures. The crossover point of the amplitudes of the superstructure and the overlayer atomic structure is by about one monolayer above the outermost layer. Around this height, the moiré pattern is clearly observed as shown in Fig. 3(c). We cannot observe directly the atomic structures of subsurfaces by STM, but can obtain information of subsurface structures by nanoscale lateral waves such as the moiré patterns.

The oscillating behavior is also seen in overlayer-thickness dependence of the superstructure amplitude. Figure 6 shows amplitudes of the superstructure calculated by Fourier transformation from (a) absolute square of a single wave function with an incident channel normal to the surface and (b) the LDOS. Values shown in the figure are calculated at a height by 5.0 a.u. above the outermost layer and are normalized by the $q=0$ component. For comparison, the amplitudes corresponding to the atomic structure of the overlayer are shown. As a matter of course, they do not depend on the overlayer thickness. When the amplitude of the superstructure is the same order as that of the atomic structure, the moiré patterns are clearly seen as shown in Fig. 4.

In the case of the single channel in Fig. 6(a), the amplitude of the superstructure does not decrease with the overlayer thickness but shows an oscillating behavior, reflecting that the superstructure wave is a propagating one. This behavior can be understood by a simple formula derived in the Appendix using the δ-function potential as

$$\sin(k_F l)\cos(k_F' l)=\frac{\sin[(k_F+k_F')l]+\sin[(k_F-k_F')l]}{2}, \tag{3.5}$$

where l is the effective overlayer thickness and is expressed as $l=(n+\delta)d$ with the number of layers in the overlayer n and the distance between the layers d. δ is a parameter of an order of 1 expressing ambiguity of the overlayer thickness. In the present case, k_F, k_F', and d are 0.290, 0.248, and 4.0, respectively. By choosing $\delta=0$, the numerical values are well fitted by this simple function.

In calculating the LDOS, many waves with various values of k_z are integrated. The superstructure amplitude decreases with the overlayer thickness like the Friedel oscillation as shown in Fig. 6(b). In this case also, the decreasing behavior can be understood by a simple formula,

$$\frac{\sin(2k_F l)-(2k_F l)\cos(2k_F l)}{(2k_F l)^2}, \tag{3.6}$$

as derived in the Appendix using the δ-function potential. Therefore, the superstructure decreases as $1/(2k_F l)$. By choosing $\delta=0.4$, the numerical values are well fitted by this formula as shown in Fig. 6(b). In Fig. 6(b), the amplitude of the superstructure shows negative values at 2, 5, 7, and 8 layers. At these overlayer thickness, the contrast of the superstructure is reversed as seen in Fig. 4(a). The superstructure contrast is sensitive to the overlayer thickness and may be used for determining the interface depth.

In the present calculation, we treat a metal surface of Cu and, therefore, the amplitude of the superstructure decreases with the overlayer thickness as shown in Fig. 6(b). In the case that there are only few states at the Fermi energy such

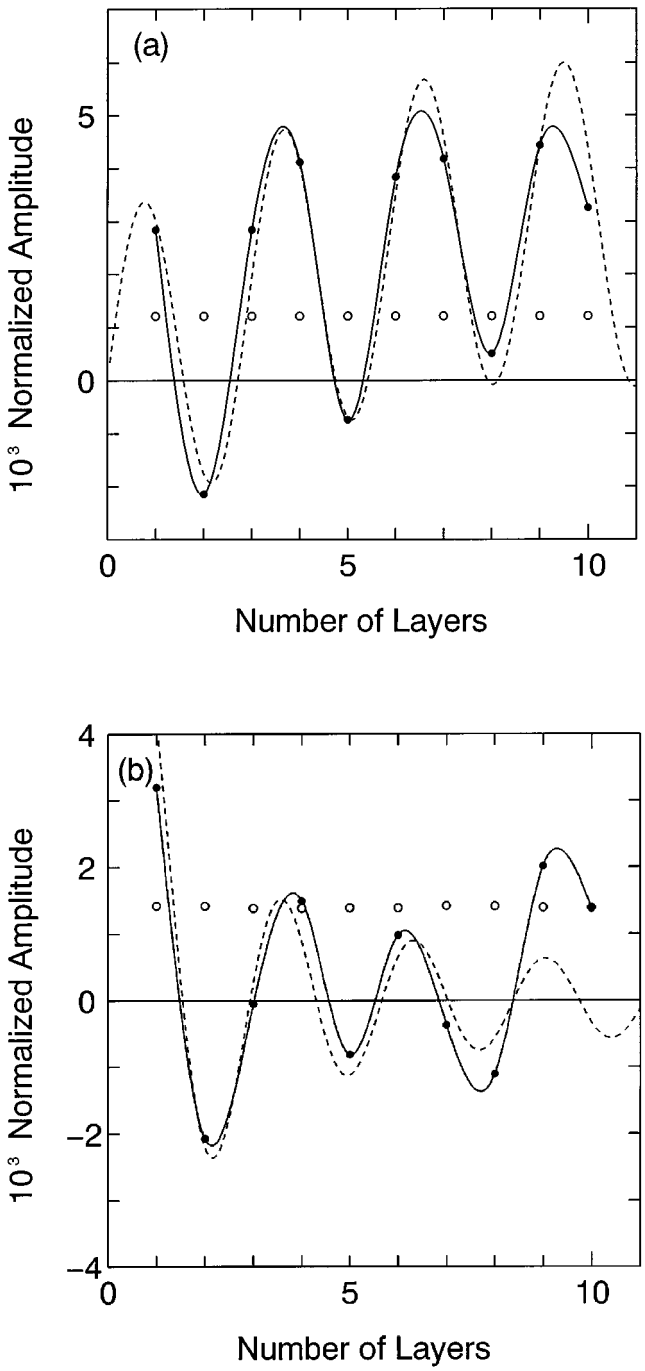

FIG. 6. Dependence of the amplitudes of the superstructure (closed circle) and the atomic structure of the outermost layer (open circle) on the overlayer thickness. The amplitudes are calculated by Fourier transformation from (a) an absolute square of a wave function with a channel of the incident wave normal to the surface and (b) the LDOS. Values are normalized by the $q=0$ component. Solid lines are obtained by spline extrapolation of the closed circles. Dotted lines show functions (a) $A\sin(k_F l)\cos(k_F' l)$ and (b) $B[\sin(2k_F l)-(2k_F l)\cos(2k_F l)]/(2k_F l)^2$, where $A=0.006$, $B=0.014$, $k_F=0.290$, and $k_F'=0.248$. The surface-interface distance l is given by $l=(n+\delta)d$, where n and d are the number of layers and the interlayer distance of the overlayer, respectively. δ is chosen as (a) 0.0 and (b) 0.4.

as graphite and semiconductors, the amplitude of the superstructure behaves like the one-channel case shown in Fig. 6(a) and does not decrease with the overlayer thickness. In such cases, it is expected that we can observe nanoscale structures buried deep in subsurfaces. This may explain the experimental fact that moiré patterns are observed even when 4 MX_2 sandwiches of the semiconducting $MoSe_2$ are grown on a MoS_2 substrate.[10]

In the above, the numerical values of the superstructure amplitudes are well fitted by the simple formulas in Eqs. (3.4)–(3.6), using only k_F and k_F', which are calculated from the spatial average of the atomic potentials in the overlayer. This means that the nanoscale waves can be treated by the effective mass theory. The nanoscale is the border length where the effective-mass theory is valid. STM can observe the waves appearing in the effective-mass theory and the atomic-scale waves simultaneously.

IV. DISCUSSION AND CONCLUSION

So far, moiré patterns in STM have been explained by the simple superposition of atomic structures of overlayers and substrates. In this picture, electrons tunnel directly from the substrates as well as the overlayers. However, this is the picture for moiré patterns in TEM and is not valid in the case of STM.

Another picture is the modulation in the electronic states of the outermost layers by the influence of the substrates. This is equivalent to the picture where on-site energies in the tight-binding model are modulated by the transfer energies between the overlayers and substrates.[23] However, the moiré patterns in STM cannot be explained by only this mechanism, because the direct influence of the substrates on the overlayers is generally very weak, as shown in Fig. 3(a). Therefore, the fact that STM makes use of the three-dimensional tunneling is important in explaining the moiré patterns. From this point of view, it is not curious that moiré patterns are observed on layered-material surfaces such as graphite[1–8] and transition-metal dichalcogenides,[9,10] where the interlayer interaction is very weak, like the van-der-Waals interaction. Moreover, the moiré patterns are observed even when several layers of overlayers are grown on the substrates, because nanoscale waves propagate through many layers without decay.

In lattice-mismatched systems, lattice distortion of overlayers induced by substrates is often important. In such cases, superstructures in STM are not so simple as the moiré patterns discussed in this paper but show domain structures.[24–31] However, the domain structures in STM are observed generally more clearly than those expected from the small amplitude of atomic displacements. These facts can be understood by the enhancement effect of nanoscale structures in STM discussed in this paper.

The mechanism of the present paper is not restricted to periodic structures such as the moiré patterns. The important point is that nanoscale structures are always enhanced in STM even when they are buried deep in subsurfaces. This would explain the large corrugation amplitudes observed in STM of bulk impurities buried in semiconductor surfaces[6–18] and of alkali-adsorbed semiconductor surfaces.[32]

In conclusion, we have clarified the mechanism of the observation of moiré patterns in STM. Different from TEM, the moiré patterns in STM is not the beat of waves and cannot be understood in terms of the simple superposition of atomic structures of overlayers and substrates. The three-dimensional tunneling and the typical value of work functions play important roles in observing nanoscale structures by STM. Moreover, we can observe nanoscale structures buried deep in subsurfaces, because nanoscale waves propagate through many layers without decay due to the typical value of Fermi energies. The mechanism presented in this paper is quite simple but general, because we often encounter nanoscale structures when we study lattice-mismatched systems synthesized by heteroepitaxy.

ACKNOWLEDGMENT

This work is partially supported by a Grant-in-Aid from the Ministry of Education, Science and Culture, Japan.

APPENDIX

In this Appendix, we derive roughly Eqs. (3.4)–(3.6) using a simple model. Since the superstructure is produced in a region localized at the interface, the scattering potential of the interface is approximated by

$$V(\mathbf{r})=v_0\delta(z)(e^{i\mathbf{q}_0\cdot\mathbf{r}_\parallel}+e^{-i\mathbf{q}_0\cdot\mathbf{r}_\parallel}), \tag{A1}$$

where v_0 is strength of the scattering potential, and $\mathbf{q}_0$ and $\mathbf{r}_\parallel$ are lateral momentum of the superstructure and coordinates parallel to the surface, respectively.

When a wave function is expanded in terms of lateral momentum $\mathbf{q}$ as

$$\psi(\mathbf{r})=\sum_{\mathbf{q}} A_{\mathbf{q}}(z)e^{i\mathbf{q}\cdot\mathbf{r}_\parallel}, \tag{A2}$$

the coefficients satisfy a relation of

$$\Delta\left(\frac{d}{dz}A_{\mathbf{q}}(z)\big|_{z=0}\right)=2v_0[A_{\mathbf{q}+\mathbf{q}_0}(0)+A_{\mathbf{q}-\mathbf{q}_0}(0)], \tag{A3}$$

where Δ means difference of values when z is approached to 0 from $+$ and $-$.

In the following, we treat the potential as a perturbation. When the unperturbed wave is

$$\psi(\mathbf{r})=e^{ikz}, \tag{A4}$$

the coefficient of the superstructure wave is determined by the condition

$$\Delta\left(\frac{d}{dz}A_{\pm\mathbf{q}_0}(z)\bigg|_{z=0}\right)=2v_0, \tag{A5}$$

and the continuity of the wave function at $z=0$. For example, when

$$A_{\mathbf{q}_0}(z)=\begin{cases} Ce^{ik'z} & (z>0) \\ Ce^{-ik'z} & (z<0) \end{cases}, \tag{A6}$$

the coefficient is determined as $C=v_0/(ik')$, where $k'=\sqrt{k^2-q_0^2}$.

In the presence of a surface at $z=l$, the unperturbed wave function changes to a standing wave as

$$\psi(\mathbf{r})=e^{ikz}+Re^{-ikz}, \quad R=-e^{2ikl}. \tag{A7}$$

The component of the superstructure $\psi_{\mathbf{q}_0}(\mathbf{r})$ produced by the δ-function potential has the form

$$\psi_{\mathbf{q}_0}(\mathbf{r})=\begin{cases}\alpha(e^{ik'z}+R'e^{-ik'z})e^{i\mathbf{q}_0\cdot\mathbf{r}_\parallel} & (z>0)\\ \beta e^{-ik'z}e^{i\mathbf{q}_0\cdot\mathbf{r}_\parallel} & (z<0),\end{cases} \tag{A8}$$

where $R'=-e^{2ik'l}$. By the condition of Eq. (A3) and the continuity, we obtain

$$\alpha=\frac{v_0}{ik'}(1+R), \qquad \beta=\alpha(1+R'). \tag{A9}$$

The $-\mathbf{q}_0$ term can be treated similarly.

The absolute square of the wave function is calculated up to the first order of the scattering potential as

$$|\psi(\mathbf{r})|^2=4\sin^2(kz)-\frac{32v_0}{k'}\sin(kl)\cos(k'l)\sin(kz) \times\sin(k'z)\cos(\mathbf{q}_0\cdot\mathbf{r}_\parallel) \quad (z>-l). \tag{A10}$$

In the above, the origin of z is changed by transforming $z-l\rightarrow z$. From this equation, we obtain the z dependence of the superstructure shown in Eq. (3.4). The oscillation term $\sin(kl)$ is originated from the interference of two waves produced by the transmitting scattering from e^{ikz} and the reflective scattering from Re^{-ikz}. Therefore, the period is governed not by k' but by k. On the other hand, the term $\cos(k'l)$ is produced by the total reflection of the superstructure itself at the surface and the period is determined by k'.

In the above, we assume that the wave function is zero at the surface, but a realistic wave function must be connected smoothly with a wave exponentially decaying in the vacuum region. The connecting points are determined by

$$k\cot(kz)=-\lambda, \qquad k'\cot(k'z)=-\lambda', \tag{A11}$$

where λ and λ' are decay constants. By putting these conditions in Eq. (A10), we obtain that the amplitude of the superstructure in the vacuum region is roughly proportional to

$$k\sin(kl)\cos(k'l), \tag{A12}$$

which is Eq. (3.5).

In calculating the LDOS, Eq. (A12) is integrated by k as

$$\int_0^{k_F}k\sin(kl)\cos(kl)dk\propto\frac{\sin(2k_Fl)-(2k_Fl)\cos(2k_Fl)}{(2k_Fl)^2}. \tag{A13}$$

In the above, we approximated $k'=k$. This is Eq. (3.6).

[1] M. Kuwabara, D. R. Clarke, and D. A. Smith, Appl. Phys. Lett. **56**, 2396 (1990).
[2] J. Xhie, K. Sattler, M. Ge, and N. Venkateswaran, Phys. Rev. B **47**, 15 835 (1993).
[3] Z. Y. Rong and P. Kuiper, Phys. Rev. B **48**, 17 427 (1993).
[4] Z. Y. Rong, Phys. Rev. B **50**, 1839 (1994).
[5] V. J. Cee, D. L. Patrick, and T. P. Beebe, Jr., Surf. Sci. **329**, 141 (1995).
[6] H. Itoh, T. Ichinose, C. Oshima, T. Ichinokawa, and T. Aizawa, Surf. Sci. **254**, L437 (1991).
[7] T. A. Land, T. Michely, R. J. Behm, J. C. Hemminger, and G. Comsa, Surf. Sci. **264**, 261 (1992).
[8] B. Nysten, J.-C. Roux, S. Flandrois, C. Daulan, and H. Saadaoui, Phys. Rev. B **48**, 12 527 (1993).
[9] F. S. Ohuchi, B. A. Parkinson, K. Ueno, and A. Koma, J. Appl. Phys. **68**, 2168 (1990).
[10] B. A. Parkinson, F. S. Ohuchi, K. Ueno, and A. Koma, Appl. Phys. Lett. **58**, 472 (1991).
[11] U. Müller, D. Carnal, H. Siegenthaler, E. Schmidt, W. J. Lorenz, W. Obretenov, U. Schmidt, G. Staikov, and E. Budevski, Phys. Rev. B **46**, 12 899 (1992).
[12] X. Bao, J. V. Barth, G. Lehmpfuhl, R. Schuster, Y. Uchida, R. Schlögl, and G. Ertl, Surf. Sci. **284**, 14 (1993).
[13] J. V. Barth, H. Brune, R. Schuster, G. Ertl, and R. J. Behm, Surf. Sci. **292**, L769 (1993).
[14] R. Strohmaier, C. Ludwig, J. Petersen, B. Gompf, and W. Eisenmenger, Surf. Sci. **318**, L1181 (1994).
[15] T. Wiederholt, H. Brune, J. Wintterlin, R. J. Behm, and G. Ertl, Surf. Sci. **324**, 91 (1995).
[16] R. M. Feenstra, J. M. Woodall, and G. D. Pettit, Phys. Rev. Lett. **71**, 1176 (1993).
[17] M. B. Johnson, O. Albrektsen, R. M. Feenstra, and H. W. M. Salemink, Appl. Phys. Lett. **63**, 2923 (1993).
[18] J. F. Zheng, X. Liu, N. Newman, E. R. Weber, D. F. Ogletree, and M. Salmeron, Phys. Rev. Lett. **72**, 1490 (1994).
[19] J. Tersoff and D. R. Hamann, Phys. Rev. Lett. **50**, 1998 (1983); Phys. Rev. B **31**, 805 (1985).
[20] M. L. Cohen and V. Heine, in *The Fitting of Pseudopotentials to Experimental Data and Their Subsequent Application*, edited by H. Ehrenreich, F. Seitz, and D. Turnbull, Solid State Physics Vol. 24 (Academic Press, New York, 1970).
[21] K. Hirose and M. Tsukada, Phys. Rev. Lett. **73**, 150 (1994); Phys. Rev. B **51**, 5278 (1995).
[22] C. J. Chen, Phys. Rev. Lett. **65**, 448 (1990).
[23] K. Kobayashi, Phys. Rev. B **50**, 4749 (1994).
[24] J. C. Patrin, Y. Z. Li, M. Chander, and J. H. Weaver, Phys. Rev. B **46**, 10 221 (1992).
[25] W. E. McMahon, E. S. Hirschorn, and T.-C. Chiang, Surf. Sci. **279**, L231 (1992).
[26] J. V. Barth, R. J. Behm, and G. Ertl, Surf. Sci. **302**, L319 (1994).
[27] C. Günther, J. Vrijmoeth, R. Q. Hwang, and R. J. Behm, Phys. Rev. Lett. **74**, 754 (1995).
[28] J. A. Meyer, P. Schmid, and R. J. Behm, Phys. Rev. Lett. **74**, 3864 (1995).

[29] M. Böhringer, P. Molinàs-Mata, E. Artacho, and J. Zegenhagen, Phys. Rev. B **51**, 9965 (1995).
[30] L. Seehofer, G. Falkenberg, D. Daboul, and R. L. Johnson, Phys. Rev. B **51**, 13 503 (1995).
[31] I.-S. Hwang, R. E. Martinez, C. Liu, and J. A. Golovchenko, Surf. Sci. **323**, 241 (1995).
[32] S. N. Magonov, H.-J. Cantow, and M.-H. Whangbo, Surf. Sci. **318**, L1175 (1994).